



Enhanced adsorption of quinoline from aqueous solution by NaOH-treated biochar derived from orange peel: preparation, performance, mechanism, and density functional theory study

Yiwei Cao, Dongyan Xu*

College of Chemical Engineering, Qingdao University of Science and Technology, Qingdao 266042, China,
email: xdy0156@qust.edu.cn (D. Xu)

Received 21 September 2023; Accepted 3 December 2023

ABSTRACT

Low-cost biochar with a large surface area and enriched oxygen functional groups was prepared by pyrolysis of orange peel and post-NaOH modification. The modified orange peel-based biochar (MOPBC) was examined for its performance in removing quinoline from aqueous solution by adsorption. As high as 197.53 mg/g of adsorption capacity of MOPBC for quinoline was achieved. The quinoline adsorption on MOPBC conforms to the pseudo-second-order kinetic model, well-fitted with the Freundlich isotherm model. Moreover, density functional theory calculation results show that quinoline is more readily adsorbed on oxygen-containing functional groups on the surface of MOPBC, especially hydroxyl groups. The plausible chemisorption mechanisms involve hydrogen bonding, acid-base interaction, π - π , and n - π interactions. This study proves that modified biochar is a prospective adsorbent concerning the disposal of quinoline in wastewater.

Keywords: Adsorption; Quinoline; Orange peel-based biochar; Mechanism; Density functional theory

1. Introduction

In the past decades, the fast growth of the coking industry has led to the massive generation of coking wastewater, which contains a large amount of non-biodegradable and hard-to-degrade organic pollutants, such as phenol, quinoline, indole, pyridine, etc. [1,2]. The discharged coking wastewater without treatment can lead to heavy natural water contamination and irreparable ecological and environmental impacts [3]. As a typical hard-to-degrade organic compound, quinoline contributes 13.47% of the total organic carbon in coking wastewater [4]. In addition, quinoline is often used as raw material and solvent for producing pesticides, pharmaceuticals, and many chemicals. Then, the development of efficient treatment technology for quinoline-containing wastewater is imminent.

Adsorption is extensively adopted to decontaminate diverse organic pollutants from water [5,6]. As the most attractive adsorbent, activated carbon demonstrates excellent adsorption capacity based on its large surface area and outstanding hydrophobicity. Recently, the use of bio-waste materials for biochar production, categorized as a renewable and cost-effective alternative to activated carbon, has been of interest in numerous studies [7,8]. For this purpose, various waste materials such as corn straw [9], sewage sludge [10], orange peel [11], wheat husk [12] and palm shells [13] have been tested as low-cost precursors for preparing biochars via pyrolysis under high temperature in the absence of oxygen. The large specific surface area, plentiful surface oxygen-containing group, high carbon content, strong adsorption capacity, and engineering adaptability have endowed biochars as a promising carbon-based adsorbent for organic contaminants removing from wastewater, showing comparable or even better performance than activated carbon [14,15].

* Corresponding author.

Biochar is a multi-porous solid product consisting primarily of microporous architecture and coexisting layered pores. The removal efficiency of targeted contaminants *via* adsorption depends highly on the physicochemical properties. Therefore, a systematic comprehension of the link between the physicochemical properties of biochar and the adsorption mechanisms has been a matter of topical interest [16,17]. Chahinez et al. [18] investigated the adsorption of crystal violet dye on palm petiole-derived biochar, proposing that pore filling, hydrogen bonding, π - π interaction, cation exchange, electrostatic attraction, and van der Waals force contribute to the adsorption. Li et al. [19] proposed that the dominant mechanisms of tetracycline in the aquatic environment on tea waste biochar are the pore-filling effect, π - π interactions, hydrogen bonds, and electrostatic interactions. The current researches are primarily concentrated on the adsorption of dyes, pharmaceuticals, pesticides, and industrial chemicals on various biochars. Yet, the currently available information on the adsorption behaviors and mechanism of quinoline on biochar is limited. Particularly, no research focuses on the theoretical explanation of the experimental results by density functional theory (DFT) for the adsorption of quinoline on biochar.

In this study, the modified orange peel-based biochar (MOPBC) was prepared by pyrolysis and activated by post-NaOH treatment, followed by characterization using N_2 adsorption, scanning electron microscopy (SEM), X-ray photoelectron spectroscopy (XPS), Raman, and Fourier-transform infrared spectroscopy (FTIR) techniques. The kinetics, isotherm, and reusability of MOPBC towards quinoline adsorption were studied in detail. Moreover, the DFT was combined with experimental studies to clarify the adsorption mechanism of quinoline over the MOPBC. The results of this study will provide directions for the design and preparation of biochar-based adsorbents.

2. Experimental set-up

2.1. Materials and characterization

The materials and characterization methods are presented in supplementary material (S1 and S2).

2.2. Preparation of orange peel-based biochar

The orange peel was first cleaned with distilled water to take away the fruit residues left on it and torn into slices for drying at 100°C for 72 h. Then, they were ground and sieved through 80 mesh sieves. 6.2 g of orange peel powder was moved into a tube furnace and held at 900°C for 1 h under an N_2 atmosphere. The obtained carbon was named orange peel-based biochar (OPBC). Then, OPBC was soaked in 0.1 M NaOH at a ratio of 100 mL/g at 25°C for 2 h under stirring. After modification, it was washed with 0.1 M HCl and distilled water to obtain a neutral pH. Finally, the biochar was obtained by drying at 110°C for 4 h and named MOPBC.

2.3. Determination of zero point of charge pH_{pzc}

The point of zero charge (pH_{pzc}) of the adsorbent surface was identified by the powder dosing method. 0.04 g

of MOPBC was added to 10 mL of 0.1 M $NaNO_3$ solution with different pH_0 values adjusted by 0.1 M H_2SO_4 and 0.1 M NaOH. The final solution pH was measured after stirring for 60 min at 25°C.

2.4. Batch adsorption study

Comprehensive details regarding the batch adsorption study are available in the supplementary materials (S3).

2.5. DFT calculations

Combined with FTIR and XPS characterization, surface structures of biochar containing different functional groups (BC-COC, BC-CO, BC-COOH and BC-OH) were constructed based on the surface structure model of 7-ring stabilized monolayer biochar. These five simplified biochar structures and quinoline molecular models were first geometrically optimized and then subjected to energy calculations. Materials Studio 2020 DMO13 software package was used for all the DFT calculations.

The adsorption energy (E_{ad}) was calculated by using Eq. (1):

$$E_{ad} = E_{A/B} - E_A - E_B \quad (1)$$

where $E_{A/B}$, E_A , and E_B are the single point energies of quinoline/biochar system, biochar, and quinoline, respectively. A negative value of E_{ad} represents exothermic adsorption.

3. Results and discussion

3.1. Characterizations of OPBC and MOPBC

Fig. 1 displays the SEM images of OPBC and MOPBC. As seen in Fig. 1a, the OPBC comprises aggregated particles of varied sizes, ranging from tens to hundreds of microns. The sample displays a sheet-like structure under high magnification (Fig. 1b). After NaOH modification, the particles became small and uniform (Fig. 1c). In addition, the MOPBC shows the appearance of 3D interconnected porous channels with non-uniform honeycomb-like morphologies on the surface (Fig. 1d). The development of this multi-pore architecture is due to the release of CO, H_2 , CO_2 , and CH_4 gases during carbonization [20].

The nitrogen adsorption and desorption measurements were performed for OPBC and MOPBC, with the textural data tabulated in Table 1. As displayed in Fig. 2a, both OPBC and MOPBC exhibit Type-I isotherm curves with the most N_2 adsorption at a relative pressure (P/P_0) below 0.1, meaning the microporous nature of these carbon materials. The microspore nature of OPBC and MOPBC was further determined by the Barrett-Joyner-Halenda pore size distribution plots, which show a complete distribution of particles with sizes less than 2 nm (inset of Fig. 2a). In addition, the alkaline treatment induced a marked increase in both specific surface area and pore volume from 784 m^2/g and 0.44 cm^3/g for OPBC to 1102 m^2/g and 0.64 cm^3/g for MOPBC, respectively. Considering that a weight loss of 20.8% occurred during the alkaline treatment, it is reasonably inferred that NaOH diffused into the micropores

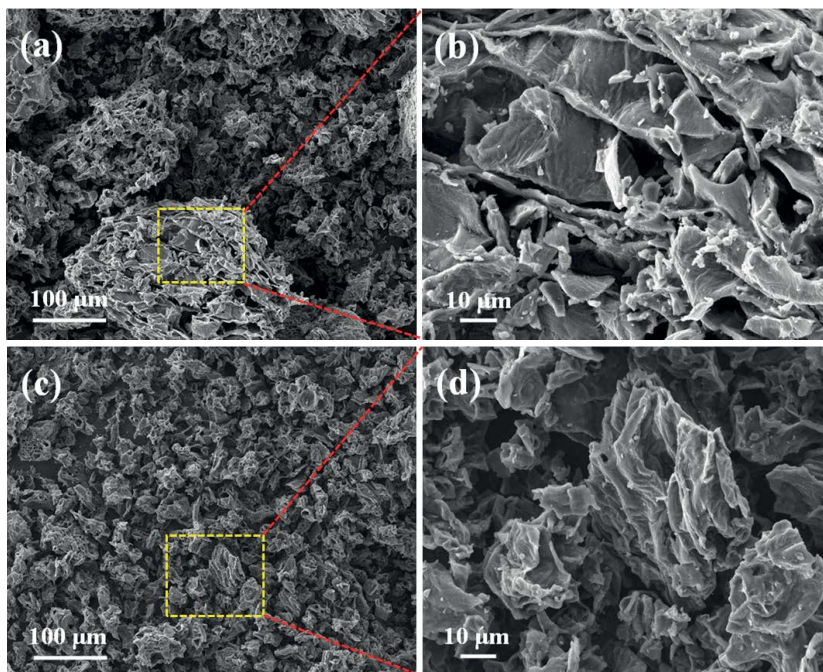


Fig. 1. Scanning electron microscopy images of OPBC (a,b) and MOPBC (c,d) at different magnifications.

Table 1
Physico-chemical properties of OPBC and MOPBC

Sample	Surface area (m ² /g)	Pore diameter (nm)	Pore volume (cm ³ /g)
OPBC	784	1.49	0.44
MOPBC	1,102	1.69	0.64

of OPBC and reacted with the ash left on the surface [21]. These reactions can cause the generation of more micropores and thus increase the specific surface area.

Fig. 2b shows qualitative information about the functional groups of OPBC and MOPBC. The similar bands of both biochars were found as follows: O–H stretching vibration (3,450 cm⁻¹) of hydroxyl groups, asymmetric C–H

stretching vibration (2,926 cm⁻¹) and symmetric C–H stretching vibration (2,853 cm⁻¹) of aliphatic groups [22], aromatic C=C stretching vibrations (1,632 cm⁻¹) [23], C–O bond of alcoholic groups and carboxylic acids (1,035 cm⁻¹), and aromatic C–H stretching vibration (800 cm⁻¹) [24]. A relatively broadband at 1,415 cm⁻¹ in OPBC is linked to C–H stretching of CH₂ and CH₃ groups, which became low intensity after NaOH treatment, indicating a decrease in the aromatic and aliphatic C–H structures due to the loss of lignin and carbohydrates [25].

XPS analysis was adopted to determine the elemental composition and the oxidation states of MOPBC. The survey spectrum of blank MOPBC shown in Fig. S1 suggests the presence of C and O. The C1s peaks of MOPBC can be fitted into four independent sub-bands at 284.8, 285.3, 287.1, and 290.3 eV (Fig. 3a), which belong to C–C/C=C/C–H, C–O/C–O–C/C–OH (i.e., amides, esters, and carboxyl moieties),

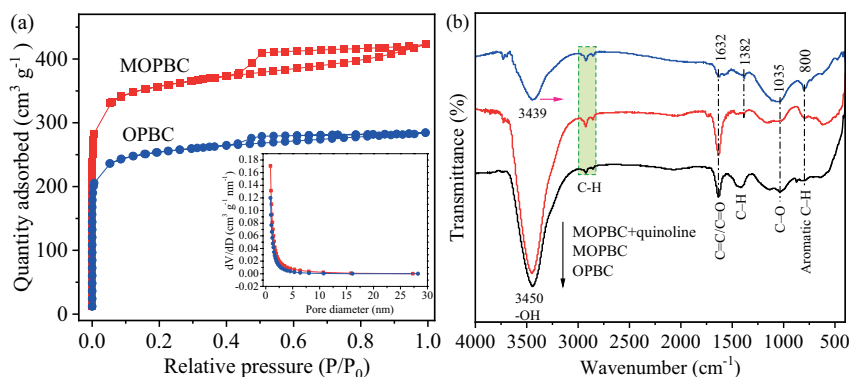


Fig. 2. (a) N₂ adsorption/desorption isotherms (inset: pore diameter distributions) of OPBC and MOPBC and (b) Fourier-transform infrared spectra of OPBC, blank MOPBC, and adsorbed MOPBC by quinoline.

C=O, and O–C=O (i.e., carboxyl or ester functionalities) bonding states [26,27]. In O1s high-resolution spectra of MOPBC (Fig. 3b), the peaks at 531.7, 532.8, and 533.9 eV indicate the existence of C=O, C–O–C/C–OH, and O=C–O functional groups [28].

The Raman spectrum of MOPBC (Fig. 3c) displays the typical broad and overlapping bands of non-graphitic carbon materials: D-band ($1,348\text{ cm}^{-1}$) associated with structural defects or disordered graphitic lattices and G-band ($1,600\text{ cm}^{-1}$) related to ideal graphitic lattices. The intensity ratio of the D and G band (I_D/I_G) is close to unity, meaning a medium degree of graphitization of MOPBC, which is beneficial to the forming π – π bonds during the adsorption of organic molecules [29].

3.2. Adsorption kinetics

The quinoline molecule measures approximately 0.7 nm in its longitudinal dimension and 0.5 nm in its axial dimension, both less than the average pore sizes of OPBC and MOPBC, and can be captured in the pores of these biochars. The adsorption capacities of OPBC and MOPBC towards quinoline were investigated under the conditions: adsorbent dosage = 2 g/L, initial quinoline concentration = 50 mg/L, 25°C, and natural solution pH = 7.0. As shown in Fig. 4a, the MOPBC displayed a substantially improved adsorption capacity compared to OPBC due to its more micropores and high Brunauer–Emmett–Teller surface area. The adsorption process is characteristic of three stages. At stage I, quinoline

molecules transferred from the aqueous solution to the outer pore tunnel of OPBC and MOPBC and adsorbed quickly on the unoccupied active sites (large π plane and oxygen functional groups) during the first 15 min. Stage II is reflected by slow adsorption because of the relatively slow transfer of quinoline molecules along the pores to access the interior pores and adsorbed on the unoccupied surface-active sites. As to the following stage III, the adsorption tends to equilibrate, with the equilibrium achieved within 100 min for OPBC and MOPBC. In this study, the highest adsorption capacity achieved by MOPBC amounted to 197.53 mg/g, outperforming other carbon-based adsorbents (Table S1).

Three kinetic models were used to fit the experimental data (Fig. 4b–d). According to the kinetic parameters in Table 2, the pseudo-second-order model showed higher R^2 values (0.993–0.999) than the pseudo-first-order model (0.892–0.972) for the entire investigated concentration range. Therefore, the adsorption of quinoline on MOPBC is primarily dominated by chemical adsorption [30]. The intraparticle diffusion model can help to determine the adsorption rate-controlling step and diffusion mechanism. The intraparticle diffusion plots show two-linearity correlations, meaning the diffusion and adsorption of quinoline experienced two sequential stages (Fig. 4d). As shown in Table 3, the first stage has good correlation coefficients (>0.933), implying that intraparticle diffusion participated in the adsorption process [31]. However, none of the C_i was zero in both adsorption stages, demonstrating that intraparticle diffusion is not the sole rate-limiting process [32]. In general, there

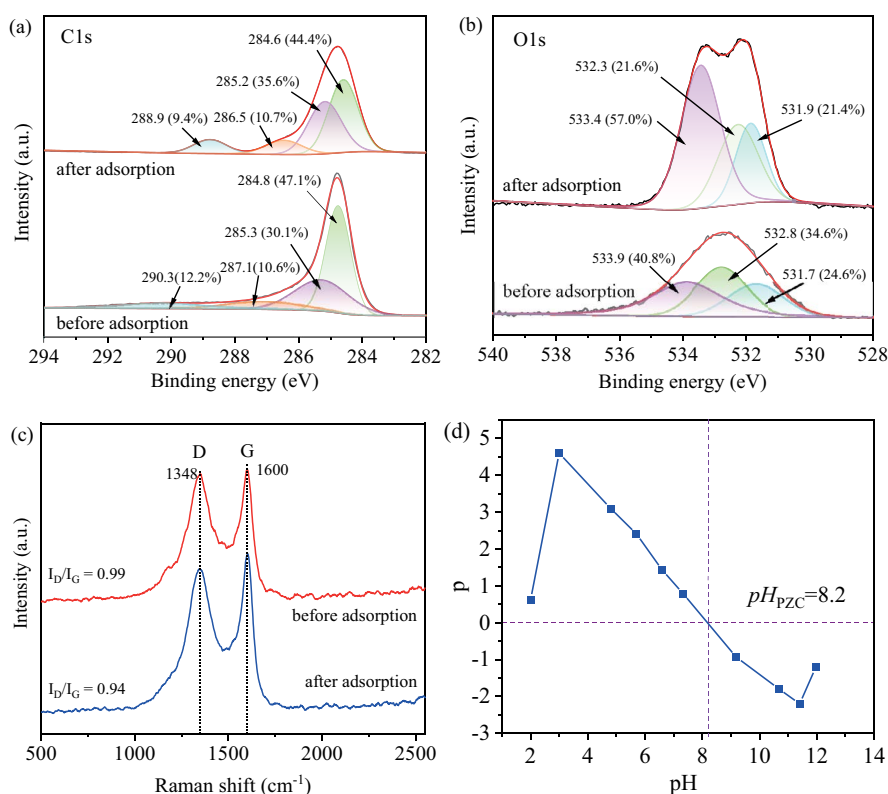


Fig. 3. X-ray photoelectron spectroscopy C1s spectra (a), X-ray photoelectron spectroscopy O1s spectra (b), and Raman spectra (c) of MOPBC before and after quinoline adsorption; point of zero charge of MOPBC (d).

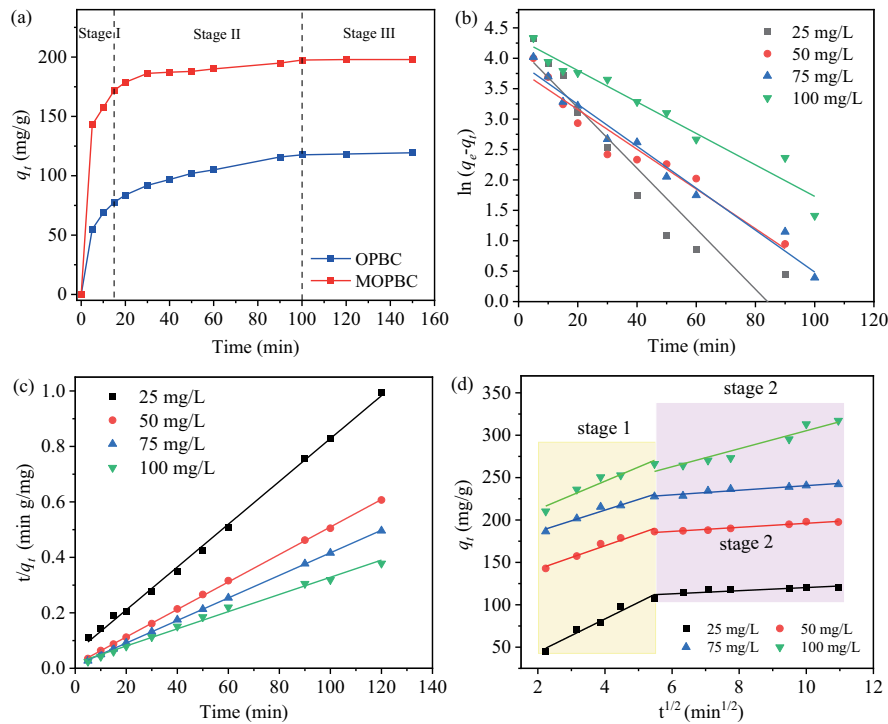


Fig. 4. (a) Adsorption of quinoline onto OPBC and MOPBC (Condition: adsorbent dosage = 2 g/L, initial quinoline concentration = 50 mg/L, $T = 25^{\circ}\text{C}$, natural pH = 7.0); linear regression plots of pseudo-first-order (b), pseudo-second-order (c), and intraparticle diffusion kinetic models (d).

Table 2

Parameters of pseudo-first-order and pseudo-second-order adsorption kinetic models at different initial quinoline concentrations

C_0 (mg/L)	$q_{e,exp}$	Pseudo-first-order model			Pseudo-second-order model		
		q_e (mg/g)	k_1 (min^{-1})	R^2	q_e (mg/g)	k_2 ($\text{g}/\text{mg}\cdot\text{min} \times 10^2$)	R^2
25	120.49	65.43	0.050	0.892	129.53	0.772	0.998
50	197.53	45.20	0.033	0.923	201.61	0.496	0.999
75	242.10	54.06	0.034	0.972	245.70	0.407	0.999
100	317.16	74.89	0.026	0.947	322.58	0.310	0.993

Table 3

Intraparticle diffusion rate constants of quinoline adsorption onto MOPBC

C_0 (mg/L)	k_1 ($\text{mg}/\text{g}\cdot\text{min}^{1/2}$)	C_1 (mg/g)	R_2^1	k_2 ($\text{mg}/\text{g}\cdot\text{min}^{1/2}$)	C_2 (mg/g)	R_2^2
25	19.535	5.13	0.967	1.850	101.82	0.730
50	13.810	114.37	0.964	2.392	172.20	0.954
75	12.607	161.21	0.955	2.710	213.40	0.934
100	16.641	179.20	0.933	10.627	199.04	0.918

is no speed limit for the diffusion of quinoline molecules from the liquid phase to the liquid–solid interface since the adsorption was carried out under strict stirring conditions [33]. During the adsorption process, boundary layer diffusion could also influence the adsorption process in some way. Therefore, the adsorption of quinoline on MOPBC involves both boundary layer diffusion and intraparticle diffusion [34,35].

3.3. Adsorption isotherm

Isotherm modeling can help elucidate the adsorption behavior and to understand the adsorption mechanism [36]. Fig. 5a presents the non-linear curves by fitting the experimental data with different isothermal adsorption models and Fig. 5b fits the linear curve isothermal adsorption models. As shown in Table 4, the fitted correlation coefficient

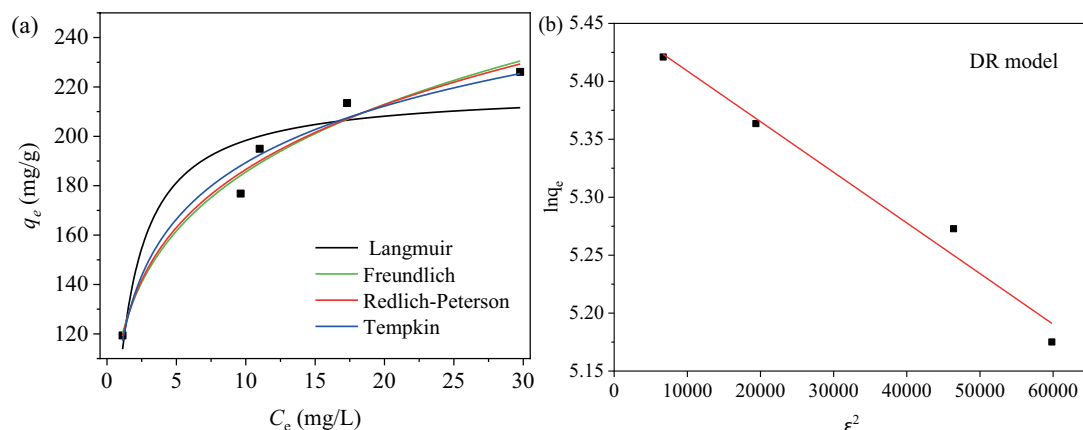


Fig. 5. Non-linear fits of equilibrium data with (a) Langmuir, Freundlich, Redlich–Peterson, Temkin and (b) Dubinin–Radushkevich isotherm models.

Table 4
Isotherm parameters for the adsorption of quinoline onto MOPBC

Model	Parameters			
	Langmuir	K_L	q_{\max}	R^2
0.96		219.01	0.857	0.034–0.480
Freundlich	K_F	$1/n$	R^2	
	117.31	0.1992	0.971	
Redlich–Peterson	K_{RP}	α	R^2	β
	1854.66	15.02	0.958	0.816
Temkin	b_T	A_T	R^2	
	74.949	30.73	0.967	
Dubinin–Radushkevich	K_D	q_{\max}	R^2	E
	4.37E-6	232.76	0.977	343.64

(R^2) of the Freundlich model is the largest, suggesting that the adsorption occurs on an energetically heterogeneous surface by multilayer adsorption [37]. The quantity of quinoline adsorbed onto adsorbent for unit equilibrium concentration is 117.31 mg/g. The value of the $1/n$ constant is lower than unity, indicating that the adsorption of quinoline onto MOPBC is favorable. Ferreira et al. [38] also found that the quinoline adsorption onto activated carbon from coconut shells conforms to the Freundlich isotherm. In the present study, through Dubinin–Radushkevich adsorption isotherm, the calculated E -value was greater than 16 kJ/mol, suggesting that the adsorption of quinoline on biochar occurs through chemisorption [39,40].

3.4. Adsorption mechanism

Previous studies proposed that multiple adsorption mechanisms might coexist. In this work, FTIR, XPS, and Raman measurements confirm the presence of potential adsorptive sites, including defects and diverse functional

groups bonded to the surfaces and edges of the aromatic rings in MOPBC. Therefore, further measuring quinoline-loaded MOPBC can help elucidate the adsorption mechanism. It is well known that quinoline is a basic nitrogen compound. Therefore, an acidic–basic interaction might occur between quinoline and acidic groups (i.e., carboxyl and phenol groups) on the surface of MOPBC, contributing much to its chemical adsorption onto adsorbent [41]. Generally, hydrogen bonds can form between quinoline molecules and the surface –OH and –COOH groups of carbon materials [42]. Furthermore, the intensity of the aromatic C=C peak at 1,632 cm^{-1} also obviously decreased, revealing a π – π interaction between the aromatic rings in quinoline and the basal graphite plane in biochar [43]. As shown in Fig. 2b, a shift of –OH stretching vibration from 3,450 to 3,439 cm^{-1} and a marked decrease in its intensity occurred after the adsorption test, indicating the existence of π – π interaction in the conjugated regions of MOPBC [44]. It was suggested that the edge sites and defects on the surface of biochar could enhance the electron-donating capacity of biochar and improve the π – π interaction [45]. The significant change in intensity of the C=O and C–O bands signified the key function of n – π interaction, which occurred between the electron-donated carbonyl oxygen ions on the surface of the adsorbent and the electron-accepted aromatic ring of quinoline. It should be emphasized that the peak that appeared at 800 cm^{-1} is ascertained to be associated with adsorbed quinoline by comprising it with the infrared spectrum of pure quinoline [46]. The new band that emerged at 1,581 cm^{-1} is possibly chemisorbed quinoline [47]. After quinoline adsorption, the C1s and O1s peaks exhibited marked variations in the intensity of these sub-bands related to oxygen-containing groups or binding energy (Fig. 3a and b). These variations further support the interaction between oxygen-containing groups and quinoline molecules. Moreover, the I_D/I_G ratio decreased from 0.99 to 0.94 after quinoline adsorption (Fig. 3c). Ahmed et al. suggested that the decrease in I_D/I_G ratio might be owing to the presence of H-bonds between surface –COOH groups of the biochar and antibiotics molecules [48].

As shown in Fig. 3d, the pH_{pzc} value of MOPBC was determined to be 8.2. Under the adsorption condition of

pH = 7, the surface of MOPBC is positively charged, while the quinoline molecules exist in cationic form with weak alkalinity. Therefore, electrostatic attraction is assumed to undertake less contribution to quinoline adsorption.

3.5. Quantum chemical calculations

The DFT calculation can be used to predict the electronic energy density of an adsorbate with BC during adsorption processes [49,50]. Fig. 6 shows the electrostatic potential (ESP) distributions of modelled BC surfaces incorporated with different oxygen functional groups and bare and BC surface. Compared with the even ESP distribution on pure BC surface, the uneven ESP distributions were induced by the presence of various oxygen functional groups. In the figure, blue color represents electrophilic sites with low electron cloud density, red color indicates nucleophilic sites with high electron cloud density, and ESP maxima and minima are circled in blue and red, respectively. As shown in Fig. 6a, the quinoline ESP ranges from -44.37 to 28.06 kcal/mol, and its negative electrostatic potential is concentrated near the nitrogen atom. As shown in Fig. 6b–f, the ESP ranges of BC, BC-CO, BC-COC, BC-COOH, and BC-OH are -13.8 – 22.73 , -42.52 – 26.79 , -36.08 – 24.58 , -36.47 – 63.82 , and -22.28 – 71.10 kcal/mol. The positive electrostatic potentials of BC-CO and BC-COC are concentrated near the hydrogen atom closest to the oxygen atom, the positive electrostatic potentials of BC-OH and BC-COOH are concentrated near the hydrogen atom of the hydroxyl group, which implies that the hydrogen atom is the site for nucleophilic attack, reasonably by the side of the nitrogen atom in quinoline. The strong electron-withdrawing ability of the oxygen atom in the oxygen-containing functional group causes the electron-transfer from the carbon atom to the oxygen atom, thus diminishing the electron cloud density around the carbon atom and rendering it positively charged. Because the positive charges of the biochar cause the formation of Lewis acid sites, the quinoline, with electron-rich nitrogen that is electronegative as

a Lewis basic site, can adsorb on the surface of MOPBC by acid–base interaction [51].

The adsorption conformation, adsorption distance and adsorption energy are shown in Fig. 7. The adsorption energies of BC, BC-CO, BC-COC, BC-COOH, and BC-OH for quinoline are -1.75 , -1.99 , -1.96 , -1.91 , and -2.27 kcal/mol, respectively, indicating that the adsorption of quinoline is a spontaneous process. Obviously, BC-CO, BC-COC, BC-COOH, and BC-OH have larger adsorption energies than BC, with the sequence of BC-OH > BC-COC > BC-CO > BC-COOH > BC. Therefore, the quinoline is more readily adsorbed on functional groups of the BC and has more stable coordination configuration. BC-OH has the highest adsorption energy, further confirming that the hydroxyl groups are the major adsorption sites of biochar [52]. Since BC-OH has a hydrogen bond donor, BC-OH can form both the hydrogen bonding and π – π interaction with quinoline simultaneously, justifying its highest adsorption energy and lowest distance between BC-OH and quinoline among the five models. In contrast, BC-CO and BC-COC lack hydrogen bond donors and can only adsorb quinoline by π – π interaction alone.

According to the experimental results and the above analysis, a rational mechanism for the adsorption of quinoline molecules by MOPBC is proposed (Fig. 8). The complexity of adsorptive sites and the presence of various adsorbent–adsorbate interactions led to the heterogeneity of the surface of MOPBC, which is coherent with the Freundlich isotherm model and the DFT calculations.

3.6. Reusability studies

Considering the practicability of the MOPBC, regeneration and recyclability of MOPBC are critical. Therefore, the recycling performance of MOPBC for quinoline removal was investigated. After each adsorption, desorption was conducted by washing the spent adsorbent in sequence with methanol, glacial acetic acid, and ethanol solution (20%) until

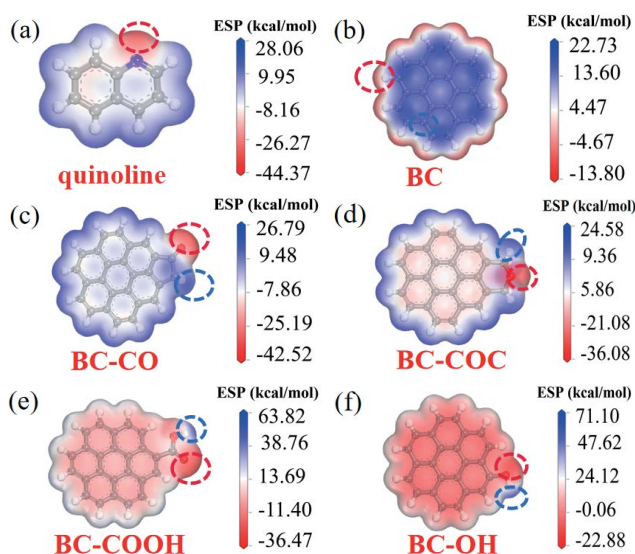


Fig. 6. Electrostatic potential distributions of quinoline (a), BC (b), BC-CO (c), BC-COC (d), BC-COOH (e) and BC-OH (f).

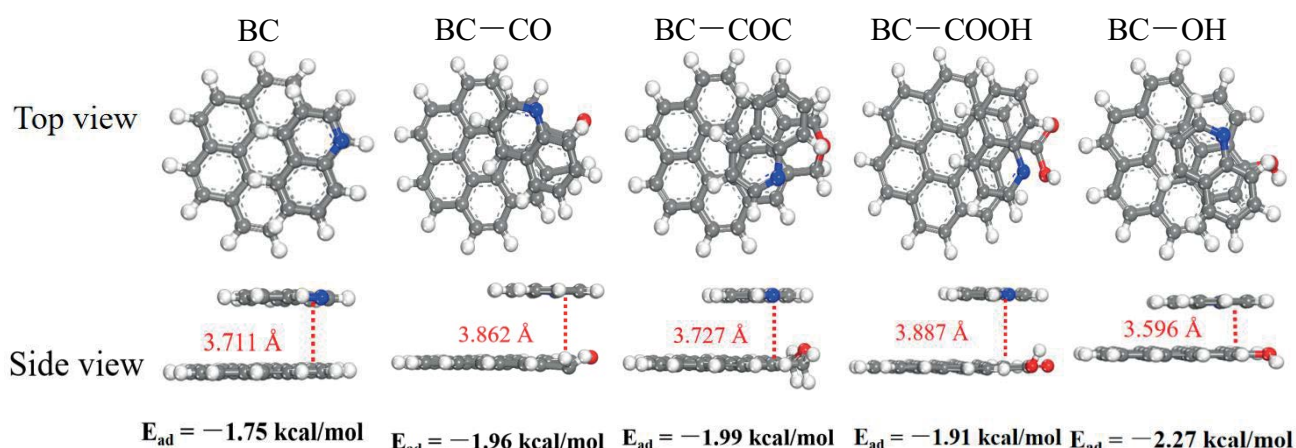


Fig. 7. Adsorption configurations of quinoline on simplified biochar structures.

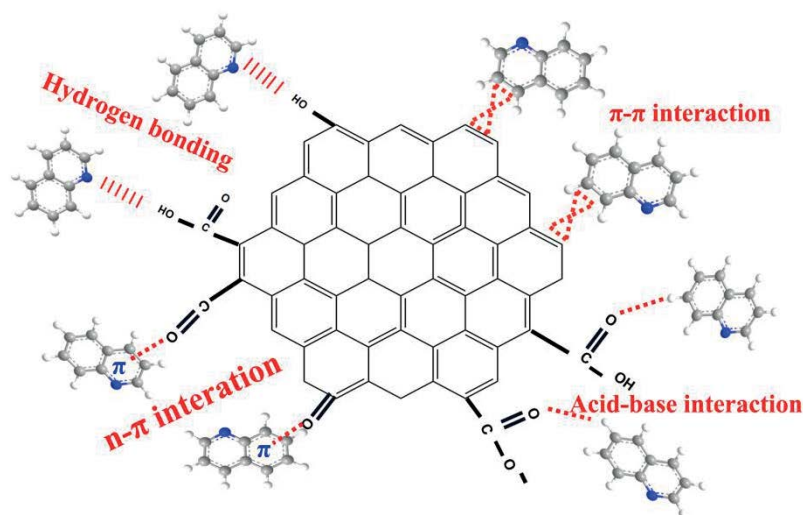


Fig. 8. Proposed synergistic chemisorption mechanism of quinoline by MOPBC.

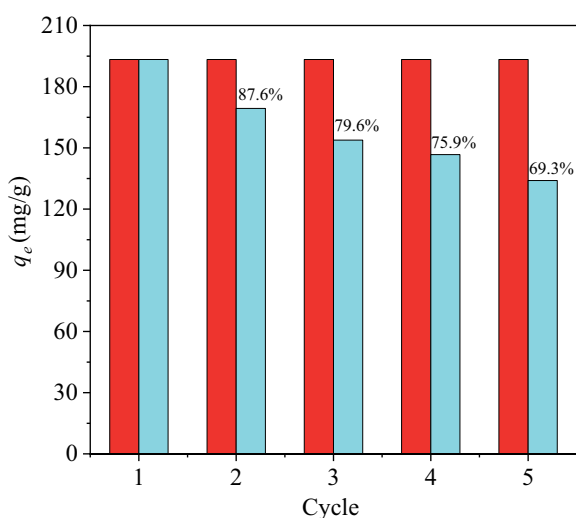


Fig. 9. Reusability of MOPBC for quinoline adsorption.

no quinoline was detected. Then, the adsorbent was dried and used for repetitive adsorption. As revealed in Fig. 9, the adsorption capacity of MOPBC for quinoline decreases from 193.35 to 134.01 mg/g after four adsorption–desorption cycles. It is inferred that some complex bond formed between the active sites of the adsorbent and the quinoline molecules, leading to incomplete desorption. The result shows that MOPBC can be used as an efficient adsorbent to remove quinoline from wastewater.

4. Conclusions

In this work, a biochar adsorbent (MOPBC) with a surface area as high as 1,102 m²/g was synthesized by pyrolysis of orange peel at 900°C and followed post-NaOH treatment. Benefiting from the high surface area and enriched surface functional groups, MOPBC achieved a higher adsorption capacity of 197.53 mg/g for quinoline than the most reported adsorbents. The adsorption of quinoline onto MOPBC obeys Freundlich isotherm and pseudo-secondary models.

Therefore, the adsorption happens on heterogenous surfaces and is chemisorption. DFT calculations indicated that the chemisorption of quinoline on MOPBC could be realized through H-bonding, acidic-basic, π - π , and n - π interactions. Additionally, the calculated adsorption energy and distance between quinoline and biochar indicate that oxygen-containing groups, especially hydroxyl groups, favor the adsorption of quinoline. Overall, MOPBC is an efficient adsorbent for applications in organic pollutant removal from water.

References

- [1] Q. Ji, S. Tabassum, S. Hena, C.G. Silva, G. Yu, Z. Zhang, A review on the coal gasification wastewater treatment technologies: past, present and future outlook, *J. Cleaner Prod.*, 126 (2016) 38–55.
- [2] H. Zhou, C. Wei, F. Zhang, J. Liao, Y. Hu, H. Wu, Energy-saving optimization of coking wastewater treated by aerobic biotreatment integrating two-stage activated carbon adsorption, *J. Cleaner Prod.*, 175 (2018) 467–476.
- [3] X. Zhang, Y. Li, Y. He, D. Kong, B. Klein, S. Yin, H. Zhao, Co-pyrolysis characteristics of lignite and biomass and efficient adsorption of magnetic activated carbon prepared by co-pyrolysis char activation and modification for coking wastewater, *Fuel*, 324 (2022) 124816, doi: 10.1016/j.fuel.2022.124816.
- [4] Z.-Y. Wu, W.-P. Zhu, Y. Liu, L.-L. Zhou, P.-X. Liu, J. Xu, An integrated biological-electrocatalytic process for highly-efficient treatment of coking wastewater, *Bioresour. Technol.*, 339 (2021) 125584, doi: 10.1016/j.biortech.2021.125584.
- [5] V. Katheresan, J. Kansedo, S.Y. Lau, Efficiency of various recent wastewater dye removal methods: a review, *J. Environ. Chem. Eng.*, 6 (2018) 4676–4697.
- [6] V.L. Gopal, K. Chellapandian, Synthesis of hybrid framework of tenorite and octahedrally coordinated aluminosilicate for the robust adsorption of cationic and anionic dyes, *Environ. Res.*, 220 (2023) 115111, doi: 10.1016/j.envres.2022.115111.
- [7] M.A. Yahya, Z. Al-Qodah, C.W.Z. Ngah, Agricultural bio-waste materials as potential sustainable precursors used for activated carbon production: a review, *Renewable Sustainable Energy Rev.*, 46 (2015) 218–235.
- [8] J. Guo, L. Zheng, Z. Li, X. Zhou, S. Cheng, Effects of various pyrolysis conditions and feedstock compositions on the physicochemical characteristics of cow manure-derived biochar, *J. Cleaner Prod.*, 311 (2021) 127458, doi: 10.1016/j.jclepro.2021.127458.
- [9] D. Xiao, Z. Hang, Q. Xiao, L. Jian, Optimization of Cd(II) removal from aqueous solution with modified corn straw biochar using Plackett–Burman design and response surface methodology, *Desal. Water Treat.*, 70 (2017) 210–219.
- [10] K. Michal, S. Bozena, U. Aleksandra, Changes of PAHs and C humic fractions in composts with sewage sludge and biochar amendment, *Desal. Water Treat.*, 97 (2017) 234–243.
- [11] K. Xiao, H. Liu, Y. Li, G. Yang, Y. Wang, H. Yao, Excellent performance of porous carbon from urea-assisted hydrochar of orange peel for toluene and iodine adsorption, *Chem. Eng. J.*, 382 (2020) 122997, doi: 10.1016/j.cej.2019.122997.
- [12] L. Esra, G. Belgin, K. Berkant, Adsorption of malachite green on Fe-modified biochar: influencing factors and process optimization, *Desal. Water Treat.*, 74 (2017) 383–394.
- [13] D.A. Usman, D.N. Noor, S.A. Noraishah, Characteristics of oil palm shell biochar and activated carbon prepared at different carbonization times, *Desal. Water Treat.*, 57 (2016) 7999–8006.
- [14] D. Akhil, D. Lakshmi, A. Kartik, D.V.N. Vo, J. Arun, K.P. Gopinath, Production, characterization, activation and environmental applications of engineered biochar: a review, *Environ. Chem. Lett.*, 19 (2021) 2261–2297.
- [15] W. Xiang, X. Zhang, J. Chen, W. Zou, F. He, X. Hu, D.C.W. Tsang, Y.S. Ok, B. Gao, Biochar technology in wastewater treatment: a critical review, *Chemosphere*, 252 (2020) 126539, doi: 10.1016/j.chemosphere.2020.126539.
- [16] T.G. Ambaye, M. Vaccari, E.D. van Hullebusch, A. Amrane, S. Rtimi, Mechanisms and adsorption capacities of biochar for the removal of organic and inorganic pollutants from industrial wastewater, *Int. J. Environ. Sci. Technol.*, 18 (2021) 3273–3294.
- [17] N. Cheng, B. Wang, P. Wu, X. Lee, Y. Xing, M. Chen, B. Gao, Adsorption of emerging contaminants from water and wastewater by modified biochar: a review, *Environ. Pollut.*, 273 (2021) 116448, doi: 10.1016/j.envpol.2021.116448.
- [18] H.O. Chahinez, O. Abdelkader, Y. Leila, H.N. Tran, One-stage preparation of palm petiole-derived biochar: characterization and application for adsorption of crystal violet dye in water, *Environ. Technol. Innovation*, 19 (2020) 100872, doi: 10.1016/j.eti.2020.100872.
- [19] B. Li, Y. Zhang, J. Xu, Y. Mei, S. Fan, H. Xu, Effect of carbonization methods on the properties of tea waste biochars and their application in tetracycline removal from aqueous solutions, *Chemosphere*, 267 (2021) 129283, doi: 10.1016/j.chemosphere.2020.129283.
- [20] R. Verma, Y.N. Singhbabu, P.N. Didwal, A.G. Nguyen, J. Kim, C.J. Park, Biowaste orange peel-derived mesoporous carbon as a cost-effective anode material with ultra-stable cyclability for potassium-ion batteries, *Batteries Supercaps*, 3 (2020) 1099–1111.
- [21] M.S. Hafizuddin, C.L. Lee, K.L. Chin, P.S. H'ng, P.S. Khoo, U. Rashid, Fabrication of highly microporous structure activated carbon *via* surface modification with sodium hydroxide, *Polymers*, 13 (2021) 3954, doi: 10.3390/polym13223954.
- [22] M.T. Vu, H.P. Chao, T. Van Trinh, T.T. Le, C.C. Lin, H.N. Tran, Removal of ammonium from groundwater using NaOH-treated activated carbon derived from corncob wastes: batch and column experiments, *J. Cleaner Prod.*, 180 (2018) 560–570.
- [23] N.S. Kumar, H.M. Shaikh, M. Asif, E.H. Al-Ghurabi, Engineered biochar from wood apple shell waste for high-efficient removal of toxic phenolic compounds in wastewater, *Sci. Rep.*, 11 (2021) 2586, doi: 10.1038/s41598-021-82277-2.
- [24] T. Cai, X. Liu, J. Zhang, B. Tie, M. Lei, Silicate-modified oiltea camellia shell-derived biochar: A novel and cost-effective sorbent for cadmium removal, *J. Cleaner Prod.*, 281 (2021) 125390, doi: 10.1016/j.jclepro.2020.125390.
- [25] P. Boguta, Z. Sokołowska, K. Skic, A. Tomczyk, Chemically engineered biochar – effect of concentration and type of modifier on sorption and structural properties of biochar from wood waste, *Fuel*, 256 (2019) 115893, doi: 10.1016/j.fuel.2019.115893.
- [26] Y. Liu, S.P. Sohi, F. Jing, J. Chen, Oxidative ageing induces change in the functionality of biochar and hydrochar: mechanistic insights from sorption of atrazine, *Environ. Pollut.*, 249 (2019) 1002–1010.
- [27] Z. Huang, L. Hu, Q. Zhou, Y. Guo, W. Tang, J. Dai, Effect of aging on surface chemistry of rice husk-derived biochar, *Environ. Prog. Sustainable Energy*, 37 (2018) 410–417.
- [28] D. Wu, F. Li, Q. Chen, M. Wu, W. Duan, Q. Zhao, B. Pan, B. Xing, Mediation of rhodamine B photodegradation by biochar, *Chemosphere*, 256 (2020) 127082, doi: 10.1016/j.chemosphere.2020.127082.
- [29] W. Yu, F. Lian, G. Cui, Z. Liu, N-doping effectively enhances the adsorption capacity of biochar for heavy metal ions from aqueous solution, *Chemosphere*, 193 (2018) 8–16.
- [30] C. Jiang, X. Wang, D. Qin, W. Da, B. Hou, C. Hao, J. Wu, Construction of magnetic lignin-based adsorbent and its adsorption properties for dyes, *J. Hazard. Mater.*, 369 (2019) 50–61.
- [31] Q. Yang, P. Wu, J. Liu, S. Rehman, Z. Ahmed, B. Ruan, N. Zhu, Batch interaction of emerging tetracycline contaminant with novel phosphoric acid activated corn straw porous carbon: adsorption rate and nature of mechanism, *Environ. Res.*, 181 (2020) 108899, doi: 10.1016/j.envres.2019.108899.
- [32] X. Li, J. Shi, X. Luo, Enhanced adsorption of rhodamine B from water by Fe-N co-modified biochar: preparation, performance, mechanism and reusability, *Bioresour. Technol.*, 343 (2022) 126103, doi: 10.1016/j.biortech.2021.126103.

- [33] P. Liao, S. Yuan, W. Xie, W. Zhang, M. Tong, K. Wang, Adsorption of nitrogen-heterocyclic compounds on bamboo charcoal: kinetics, thermodynamics, and microwave regeneration, *J. Colloid Interface Sci.*, 390 (2013) 189–195.
- [34] D. Balarak, M. Baniasadi, S.M. Lee, M.L. Shim, Ciprofloxacin adsorption onto *Azolla filiculoides* activated carbon from aqueous solutions, *Desal. Water Treat.*, 218 (2021) 444–453.
- [35] D. Balarak, A.H. Mahvi, M.J. Shim, S.M. Lee, Adsorption of ciprofloxacin from aqueous solution onto synthesized NiO: isotherm, kinetic and thermodynamic studies, *Desal. Water Treat.*, 212 (2021) 390–400.
- [36] M.A. Al-Ghouti, D.A. Da'ana, Guidelines for the use and interpretation of adsorption isotherm models: a review, *J. Hazard. Mater.*, 393 (2020) 122383, doi: 10.1016/j.jhazmat.2020.122383.
- [37] S. Parimal, M. Prasad, U. Bhaskar, Prediction of equilibrium sorption isotherm: comparison of linear and non-linear methods, *Ind. Eng. Chem. Res.*, 49 (2010) 2882–2888.
- [38] M.E. de Oliveira Ferreira, B.G. Vaz, C.E. Borba, C.G. Alonso, I.C. Ostroski, Modified activated carbon as a promising adsorbent for quinoline removal, *Microporous Mesoporous Mater.*, 277 (2019) 208–216.
- [39] F.K. Mostafapour, M. Yilmaz, A.H. Mahvi, A. Younesi, F. Ganji, D. Balarak, Adsorptive removal of tetracycline from aqueous solution by surfactant-modified zeolite: equilibrium, kinetics and thermodynamics, *Desal. Water Treat.*, 247 (2022) 216–228.
- [40] F.K. Mostafapour, A.H. Mahvi, A.D. Khatibi, M.K. Saloot, N. Mohammadzadeh, D. Balarak, Adsorption of lead(II) using bioadsorbent prepared from immobilized *Gracilaria corticata* algae: thermodynamics, kinetics and isotherm analysis, *Desal. Water Treat.*, 265 (2022) 103–113.
- [41] J.H. Kim, X. Ma, A. Zhou, C. Song, Ultra-deep desulfurization and denitrogenation of diesel fuel by selective adsorption over three different adsorbents: a study on adsorptive selectivity and mechanism, *Catal. Today*, 111 (2006) 74–83.
- [42] W. Kang, Y. Cui, Y. Yang, M. Guo, Z. Zhao, X. Wang, X. Liu, Preparation of nitrogen-doped hollow carbon nanosphere/graphene composite aerogel for efficient removal of quinoline from wastewater, *J. Hazard. Mater.*, 417 (2021) 126160, doi: 10.1016/j.jhazmat.2021.126160.
- [43] D. Zhu, H. Jiang, L. Zhang, X. Zheng, H. Fu, M. Yuan, H. Chen, R. Li, Aqueous phase hydrogenation of quinoline to decahydroquinoline catalyzed by ruthenium nanoparticles supported on glucose-derived carbon spheres, *ChemCatChem*, 6 (2014) 2954–2960.
- [44] S. Yu, X. Wang, Y. Ai, X. Tan, T. Hayat, W. Hu, X. Wang, Experimental and theoretical studies on competitive adsorption of aromatic compounds on reduced graphene oxides, *J. Mater. Chem., A*, 4 (2016) 5654–5662.
- [45] D. Yang, J. Li, L. Luo, R. Deng, Q. He, Y. Chen, Exceptional levofloxacin removal using biochar-derived porous carbon sheets: mechanisms and density-functional-theory calculation, *Chem. Eng. J.*, 387 (2020) 124103, doi: 10.1016/j.cej.2020.124103.
- [46] T.J. Dines, L.D. MacGregor, C.H. Rochester, IR spectroscopic investigation of the interaction of quinoline with acidic sites on oxide surfaces, *Langmuir*, 18 (2002) 2300–2308.
- [47] L. Zhang, X. Wang, Y. Xue, X. Zeng, H. Chen, R. Li, S. Wang, Cooperation between the surface hydroxyl groups of Ru-SiO₂@mSiO₂ and water for good catalytic performance for hydrogenation of quinoline, *Catal. Sci. Technol.*, 4 (2014) 1939–1948.
- [48] M.B. Ahmed, J.L. Zhou, H.H. Ngo, W. Guo, M.A.H. Johir, K. Sornalingam, Single and competitive sorption properties and mechanism of functionalized biochar for removing sulfonamide antibiotics from water, *Chem. Eng. J.*, 311 (2017) 348–358.
- [49] K. Jeyasubramanian, B. Thangagiri, A. Sakthivel, R. Dhavethu, J. Seenivasan, S. Vallinayagam, P. Madhavan, D. Malathi, A complete review on biochar: production, property, multifaceted applications, interaction mechanism and computational approach, *Fuel*, 292 (2021) 120243, doi: 10.1016/j.fuel.2021.120243.
- [50] L. Liu, Z. Yang, F. Zhao, Z. Chai, W. Yang, H. Xiang, Z. Lin, Manganese doping of hematite enhancing oxidation and bidentate-binuclear complexation during As(III) remediation: experiments and DFT calculation, *Chem. Eng. J.*, 471 (2023) 144758, doi: 10.1016/j.cej.2023.144758.
- [51] S. Zhao, Y. Zhang, DFT study on the chemisorption and reforming of naphthalene over biochar: the detailed mechanism of carbon deposition and hydrogen production, *Fuel*, 332 (2023a) 126144, doi: 10.1016/j.fuel.2022.126144.
- [52] H. Zhao, Z. Wang, Y. Liang, T. Wu, Y. Chen, J. Yan, Y. Zhu, D. Ding, Adsorptive decontamination of antibiotics from livestock wastewater by using alkaline-modified biochar, *Environ. Res.*, 226 (2023b) 115676, doi: 10.1016/j.envres.2023.115676.

Supporting information

S1. Materials

All chemicals used in this study were of analytical grade. NaOH (≥99%) and NaNO₃ (≥99%) were purchased from Tianjin Hengxing Chemical Reagent Manufacturing Co., (China). H₂SO₄ (≥99%) was purchased from Laiyang Economic and Technological Development Zone Fine Chemical Plant. HCl (≥99%) was purchased from Yantai Sanhe Chemical Reagent Co., (China). Quinoline (≥99%) was purchased from Tianjin Beilian Fine Chemicals Development Co., (China). Anhydrous methanol and anhydrous ethanol (≥99.7%) were purchased from Sinopharm Group Chemical Reagent Co., (China). Glacial acetic acid (≥99.7%) was purchased from Shanghai Aladdin Biochemical Technology Co., (China). Orange peel waste was collected from a supermarket in Qingdao, China.

S2. Characterizations

The morphology of the orange peel-based biochar and MOPBC was measured with SEM (JSM-6700F, Japan). The N₂ adsorption–desorption isotherms were carried out at 77 K on a surface area analyzer (Micromeritics, ASAP 2020, USA). The surface area was estimated by the Brunauer–Emmett–Teller method. Fourier-transform infrared spectroscopy was performed on a Bruker Tensor 27 spectrometer (Germany). X-ray photoelectron spectroscopy was performed on a Thermo ESCALAB 250Xi spectrometer (USA). The binding energy calibrated at C1s 284.8. The Raman spectra were recorded on an inVia Qontor spectrometer (Renishaw, UK).

S3. Adsorption experiments

In a typical batch adsorption experiment, 0.01 g of adsorbent was added to 50 mL of quinoline solution with an initial concentration of 50 mg/L and maintained in a 100 mL glass bottle for the time corresponding to the analysis. The glass bottles were placed in a constant temperature hydrothermal magnetic stirrer (DF-101S collector-type). All the adsorption experiments were conducted at the initial pH of the quinoline solution (7 ± 0.2). After adsorption, the samples were drawn at specified time intervals and the adsorbents were separated with a 0.45 μm polytetrafluoroethylene syringe membrane filter, and the filtrate solution was analyzed for obtaining the remaining concentration of quinoline. The kinetic experiments were carried out by varying the initial quinoline concentration (25–100 mg/L), solution temperature

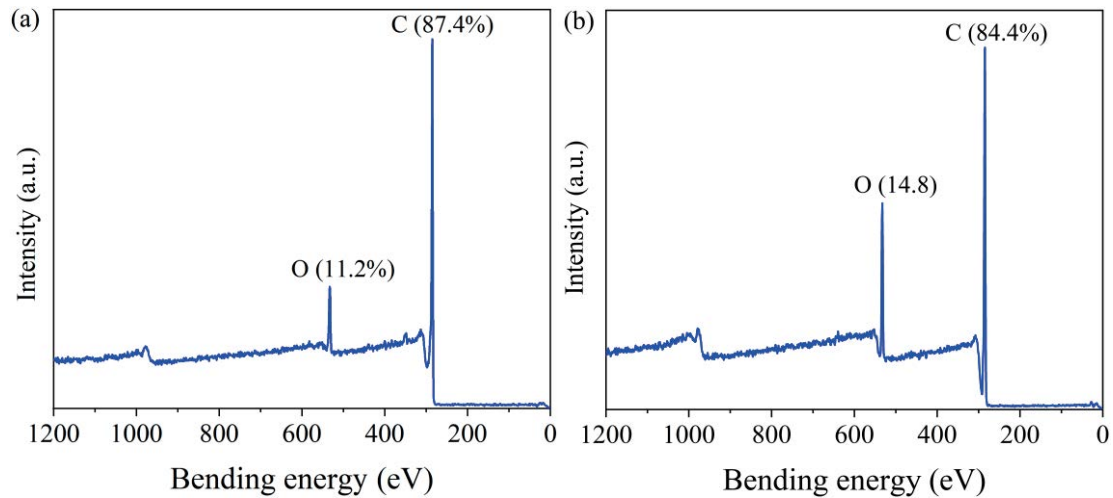


Fig. S1. X-ray photoelectron spectroscopy survey spectra of MOPBC before (a) and after (b) quinoline adsorption.

Table S1

Comparison of the q_e values of quinoline adsorbed by different carbon adsorbents

Absorbent	T ($^{\circ}\text{C}$)	C_0 (mg/L)	Adsorbent dosage (g/L)	q_{max} (mg/g)	References
Granular activated carbon	30	50	5	8.78	[S1]
Mesoporous N-doped carbon	30	0.5	6	16.66	[S2]
Magnetic carbon nanospheres	25	50	0.5	99.43	[S3]
Carbon from coconut shell	30	2,800	66.67	56.63	[S4]
Modified agricultural waste	5	100	5	35.0	[S5]
Carbon from walnut shells	40	120	1	166.91	[S6]
Magnetic hollow carbon nanospheres	25	50	0.5	155.23	[S7]
Activated carbon modified with $(\text{NH}_4)_2\text{S}_2\text{O}_8$	25	0.3	0.5	35.7	[S8]
Biochar from orange peel	25	50	0.2	197.53	This work

(25 $^{\circ}\text{C}$ –45 $^{\circ}\text{C}$), and adsorbent dosage (0.1–1 g/L), respectively. The remaining concentrations of quinoline were determined by a UV752 UV-Visible Spectrophotometer (Yoke, China) at the wavelength of 280 nm using a calibration curve.

The equilibrium adsorption capacity (q_e) and time-dependent adsorption capacity (q_t) are calculated by Eqs. (S1) and (S2):

$$q_e = \frac{V(C_0 - C_e)}{m} \quad (\text{S1})$$

$$q_t = \frac{V(C_0 - C_t)}{m} \quad (\text{S2})$$

where C_0 , C_t and C_e are the initial, time-dependent and equilibrium quinoline concentrations (mg/L), respectively. V (L) is the volume of solution and m (g) is the adsorbent amount.

References

- [S1] D. Rameshraj, V.C. Srivastava, J.P. Kushwaha, I.D. Mall, Quinoline adsorption onto granular activated carbon and bagasse fly ash, *Chem. Eng. J.*, 181–182 (2012) 343–351.
- [S2] X. Yu, R. Nie, H. Zhang, X. Lu, D. Zhou, Q. Xia, Ordered mesoporous N-doped carbon supported Ru for selective adsorption and hydrogenation of quinoline, *Microporous Mesoporous Mater.*, 256 (2018) 10–17.
- [S3] Y. Cui, L. Qin, W. Kang, J. Ma, Y. Yang, X. Liu, Magnetic carbon nanospheres: synthesis, characterization, and adsorbability towards quinoline from coking wastewater, *Chem. Eng. J.*, 382 (2020) 122995, doi: 10.1016/j.cej.2019.122995.
- [S4] M.E. de Oliveira Ferreira, B.G. Vaz, C.E. Borba, C.G. Alonso, I.C. Ostroski, Modified activated carbon as a promising adsorbent for quinoline removal, *Microporous Mesoporous Mater.*, 277 (2019) 208–216.
- [S5] M.J.K. Ahmed, M. Ahmaruzzaman, Investigation on the effective remediation of quinoline at solid/solution interface using modified agricultural waste: an inclusive study, *Int. J. Environ. Sci. Technol.*, 13 (2016) 1177–1188.
- [S6] T. Yang, X. Hu, P. Zhang, X. Chen, W. Wang, Y. Wang, Q. Liang, Y. Zhang, Q. Huang, Study of pre-treatment of quinoline in aqueous solution using activated carbon made from low-cost agricultural waste (walnut shells) modified with ammonium persulfate, *Water Sci. Technol.*, 79 (2019) 2086–2094.
- [S7] Y. Cui, W. Kang, L. Qin, J. Ma, X. Liu, Y. Yang, Ultrafast synthesis of magnetic hollow carbon nanospheres for the adsorption of quinoline from coking wastewater, *New J. Chem.*, 44 (2020) 7490–7500.
- [S8] X. Feng, X. Ma, N. Li, C. Shang, X. Yang, X.D. Chen, Adsorption of quinoline from liquid hydrocarbons on graphite oxide and activated carbons, *RSC Adv.*, 5 (2015) 74684–74691.